Imaging-Assisted Single-Photon Doppler-Free Laser Spectroscopy and the Ionization Energy of Metastable Triplet Helium

Gloria Clausen,[1] Simon Scheidegger,[1] Josef A. Agner,[1] Hansjürg Schmutz,[1] and Frédéric Merkt[1,2,3]
[1]Department of Chemistry and Applied Biosciences, ETH Zurich, CH-8093 Zurich, Switzerland
[2]Quantum Center, ETH Zurich, CH-8093 Zurich, Switzerland
[3]Department of Physics, ETH Zurich, CH-8093 Zurich, Switzerland

(Received 7 June 2023; revised 21 July 2023; accepted 14 August 2023; published 5 September 2023)

Skimmed supersonic beams provide intense, cold, collision-free samples of atoms and molecules and are one of the most widely used tools in atomic and molecular laser spectroscopy. High-resolution optical spectra are typically recorded in a perpendicular arrangement of laser and supersonic beams to minimize Doppler broadening. Typical Doppler widths are nevertheless limited to tens of MHz by the residual transverse-velocity distribution in the gas-expansion cones. We present an imaging method to overcome this limitation that exploits the correlation between the positions of the atoms and molecules in the supersonic expansion and their transverse velocities, and thus their Doppler shifts. With the example of spectra of $(1s)(np)\,^3P_{0-2} \leftarrow (1s)(2s)\,^3S_1$ transitions to high Rydberg states of metastable triplet He, we demonstrate the suppression of the residual Doppler broadening and a reduction of the full linewidths at half maximum to only about 1 MHz in the UV. Using a retroreflection arrangement for the laser beam and a cross-correlation method, we determine Doppler-free spectra without any signal loss from the selection, by imaging, of atoms within ultranarrow transverse-velocity classes. As an illustration, we determine the ionization energy of triplet metastable He and confirm the significant discrepancy between recent experimental [G. Clausen *et al.*, Phys. Rev. Lett. **127**, 093001 (2021)] and high-level theoretical [V. Patkós *et al.*, Phys. Rev. A **103**, 042809 (2021)] values of this quantity.

DOI: 10.1103/PhysRevLett.131.103001

Atoms and molecules absorb and emit radiation at frequencies that appear shifted to higher or lower frequencies depending on whether they move towards or away from the observer. This effect is known as the Doppler effect and leads to a broadening of spectral lines in atomic and molecular spectra that reflects the velocity distribution of the sample of absorbing or emitting atoms and molecules. This line broadening represents a major challenge in high-resolution spectroscopy [1]. Efforts towards eliminating Doppler broadening in atomic and molecular spectroscopy have a long history [2] and can be classified in three categories. The first consists in reducing the spread of the velocity distribution in the direction of the observer by cooling the gas or forming a collimated gas beam. Remarkable examples in this category include full resolution of the rotational structure in the IR spectrum of C_{60} after buffer-gas cooling [3] and precision-spectroscopic studies of free radicals in supersonic expansions [4]. In the second approach, referred to as sub-Doppler spectroscopy, spectra are recorded after selection of a subset of atoms or molecules belonging to a narrow velocity class out of the sample, for instance, through double-resonance methods, resonant multiphoton excitation, and saturation spectroscopy [5], or through the detection of spatially resolved fluorescence [6]. Recent examples include precision measurements of rovibrational transitions in CH_4 [7] and H_2O [8]. In sub-Doppler spectroscopy, only a fraction of the sample contributes to the line intensities, which reduces the sensitivity. In the third approach, the Doppler shifts are canceled through two-photon absorption from two counterpropagating laser beams of the same frequency. The measurements are thus Doppler-free. Precision measurements of the $1s$-$2s$ transition frequency in H are the best examples in this category [9,10]. The great advantage of this approach beyond the elimination of the Doppler width is that all atoms or molecules in the sample contribute to the intensity of the Doppler-free lines, regardless of their velocity. Recent developments have combined two-photon Doppler-free spectroscopy with Ramsey-comb interferometry [11] and broadband Fourier-transform dual-comb spectroscopy [12]. So far, no equivalent approach has been established for single-photon spectroscopy. The purpose of this Letter is to fill this gap and introduce a method to record optical spectra with the best possible signal-to-noise ratio and spectral resolution.

The method exploits the correlation between the positions and velocities of atoms or molecules in an expanding gas sample and is schematically illustrated in Fig. 1 with the example of the supersonic expansion used here as demonstration. The free expansion of the supersonic beam leads to a distribution of transverse velocities along the laser propagation axis with position-specific Doppler shifts

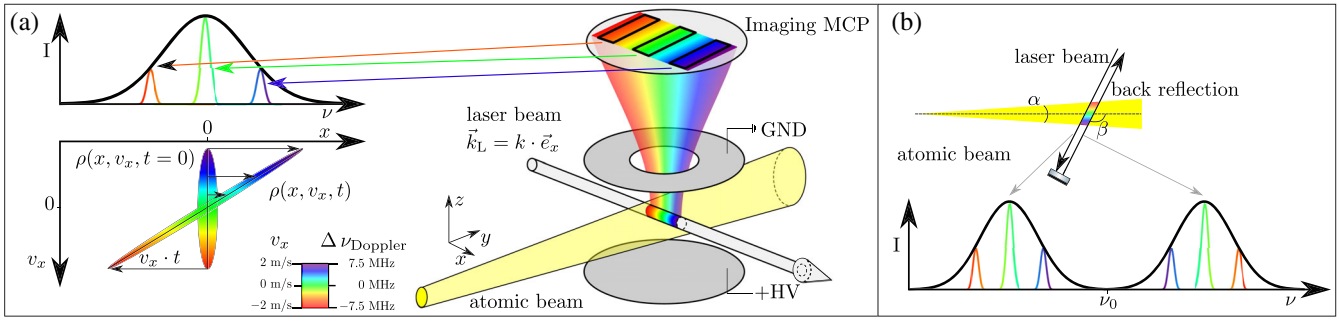

FIG. 1. Principle of imaging-assisted sub-Doppler spectroscopy in supersonic beams. (a) Experimental geometry exploiting the correlation between the transverse velocities of the atoms and their positions along the laser beam, illustrated by the phase-space diagram. This correlation leads to Doppler-shift-dependent photoexcitation spots, symbolized by the rainbow-color scheme, which are imaged following perpendicular extraction of the ions generated by pulsed-field ionization. (b) Determination of the Doppler-free transition frequency following inversion of the Doppler shifts upon retroreflection of the laser beam. An intentional slight deviation from 90° of the angle β between the atomic and laser beams leads to pairs of lines with opposite Doppler shifts and a first-order-Doppler-free frequency ν_0.

of the atomic or molecular transition frequencies indicated by the rainbow-color scheme. The corresponding phase-space evolution $\rho(x, v_x, t)$ is also represented schematically in Fig. 1(a). Pulsed-field ionization (PFI) (or ionization with a second photon) of the upper level of the transition leads to the generation of ions at positions determined by the Doppler shifts. Extraction of the ions with a homogeneous-electric-field pulse towards a microchannel-plate (MCP) detector connected to a charge-coupled-device (CCD) camera is used to spatially image [13] the generated ion cloud. The detection positions of the ions on the image are correlated to the Doppler shifts. Monitoring the ionization signal in selected areas of the image (indicated by rectangles) as a function of the laser frequency enables the recording of spectra with sub-Doppler linewidths (colored lines in the top left spectrum). To determine the Doppler-free transition frequency, the laser propagation axis is chosen not to be exactly perpendicular to the gas-beam axis (intersection angle $\beta \approx 89.5°$) and is retroreflected by a mirror located beyond the gas beam, which inverts the Doppler shifts and leads to pairs of lines [Fig. 1(b)]. The Doppler-free transition frequency ν_0 is the average of the frequencies of the pair of corresponding sub-Doppler lines. A cross-correlation method is then used to combine all sub-Doppler spectra in a single Doppler-free spectrum of the full sample. In this Letter, we demonstrate this method with a proof-of-principle measurement of the $(1s)(np)\,^3P_J \leftarrow (1s)(2s)\,^3S_1$ transitions in ^{4}He.

The experimental setup is displayed schematically in Fig. 2 and has been described earlier [14]. A supersonic beam of helium atoms with velocities around 480 m/s is generated from a high-pressure reservoir emitting helium atoms into vacuum by a pulsed valve (repetition rate 8.33 Hz) cooled to 12 K. A dielectric-barrier discharge at the nozzle orifice excites ^{4}He to the metastable $(1s)(2s)\,^3S_1$ state (He* hereafter). Transversely cold He* is selected with a 1-mm-diameter skimmer placed in a distance of 45 cm from the valve orifice. The skimmed atomic beam enters the interaction region 1.35 m downstream from the skimmer, where it is intersected by a single-mode continuous-wave UV laser beam ($\lambda \approx 260$ nm, waist diameter of 1.2 mm, power ≈10 mW) at near-right angles to excite np Rydberg states. The transitions are detected by PFI of the Rydberg states and extraction of the ^{4}He$^+$ ions toward an MCP imaging detector in the direction perpendicular to the atomic and laser beams (z axis). The

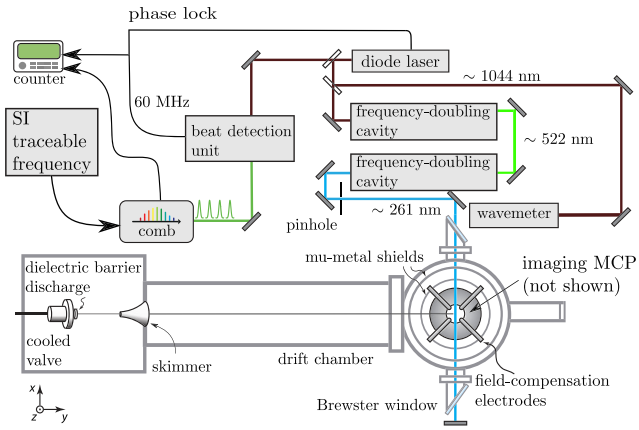

FIG. 2. Schematic diagram of the experimental setup. Top: Laser system including the single-mode frequency-quadrupled diode laser used to photoexcite He* to high Rydberg states and the frequency-comb-based SI-traceable frequency-calibration system. Bottom: Valve and discharge electrodes used to generate the supersonic expansion of He*, drift chamber, and photoexcitation chamber, where the atomic and laser beams cross on the axis of a set of cylindrical electrodes used to field ionize the Rydberg states and extract the He$^+$ ions towards an imaging microchannel-plate detector within a double-layer mu-metal magnetic shield and electrodes for three-dimensional electric-stray-field compensation.

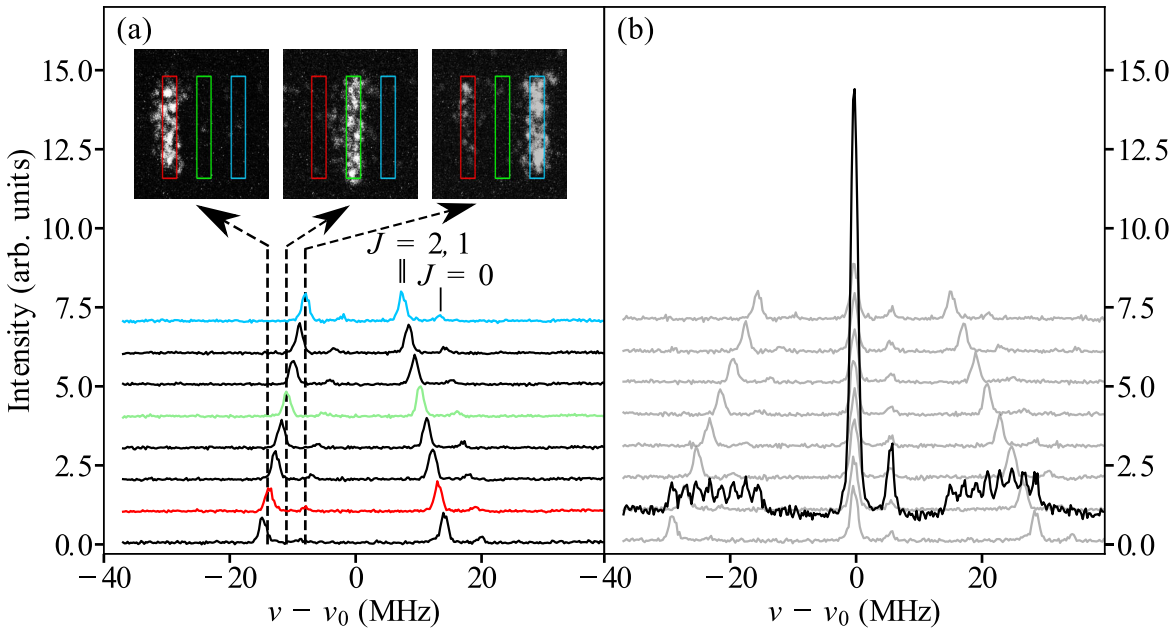

FIG. 3. (a) Sub-Doppler spectra of the $(1s)(33p)\,^3P_{0-2} \leftarrow (1s)(2s)\,^3S_1$ transitions in He recorded in adjacent areas of the imaging detector. The insets present the images recorded at the frequencies marked by dashed vertical lines for the three sub-Doppler spectra highlighted in red, green, and blue. (b) Gray: Cross-correlation spectra between the individual sub-Doppler spectra and synthetic spectra consisting of two Dirac delta distributions separated by the corresponding Doppler shift. Black: Sum of the cross-correlation spectra revealing the sharp Doppler-free transitions and their weak Doppler-broadened side bands.

photoexcitation region is magnetically shielded using two concentric mu-metal shields. Stray electric fields are compensated to below 1 mV/cm in all three spatial directions using a stack of plane electrodes in the z direction and four pin electrodes in the x and y directions [14].

The phosphorescence of the imaging MCP is detected with a CCD camera. The resulting image is divided into adjacent detection areas along the direction of the laser beam [see Fig. 1(a)]. Spectra of the $(1s)(np)\,^3P_J \leftarrow (1s)(2s)\,^3S_1$ transition are recorded by scanning the laser frequency, collecting the ions impinging on each of the detection areas separately, and monitoring the corresponding integrated signals.

The UV radiation is generated from the output of a tapered-amplifier diode laser at 1040 nm, which is frequency quadrupled using two doubling cavities equipped with nonlinear frequency-upconversion crystals. A 1% reflection of the laser beam is used to reduce the laser linewidth to $\ll 80$ kHz by a phase lock to an optical ultra-low-noise frequency comb (*FC1500-250-ULN, Menlo Systems*). The 1040 nm laser is frequency shifted with an acousto-optic modulator (AOM) operated in a double-pass configuration, allowing one to scan the fundamental laser frequency with respect to the frequency comb. The comb itself is short-term stabilized by a 1572-nm laser locked to a high-finesse cavity. Long-term drifts are detected by referencing the frequency comb to an ultra-stable and SI-traceable frequency disseminated by the stabilized fiber network described in Ref. [15]. The UV laser frequency is scanned in discrete steps $\Delta\nu$ (typically $\Delta\nu = 240$ kHz) and, at each step, the data are averaged over 75 experimental cycles. To cancel the first-order Doppler shift, the laser beam is retroreflected and a distant pinhole is used to ensure a reflection angle within $180.00 \pm 0.03°$.

Figure 3(a) illustrates the measurement procedure with spectra of the $(1s)(33p)\,^3P_{0-2} \leftarrow (1s)(2s)\,^3S_1$ transitions obtained from eight adjacent detector regions. For clarity, the different spectra were shifted along the y axis according to the spatial ordering of the detection areas. The spin-orbit interaction splits the $33p$ triplet state into three components with $J = 0$–2, two of which ($J = 1$, 2) are almost degenerate, as assigned in the top spectrum of Fig. 3(a) [16]. Each spectrum consists of two Doppler components having opposite first-order Doppler shifts. Because each selected area of the images corresponds to a specific transverse-velocity class, the splitting between the Doppler components evolves from one spectrum to the next.

The three images presented as insets in Fig. 3(a) illustrate the efficacy of the selection of narrow velocity classes. They were recorded at the frequencies corresponding to the vertical dashed lines. At the lowest of these frequencies, the He^+ ions are detected on the left of the image in the area used to record the spectrum drawn in red. At the middle frequency, the He^+ ions are detected near the image center in the area used to record the spectrum drawn in green. In both cases, the detected He^+ ions result from PFI of Rydberg atoms in the $J = 1$, 2 fine-structure components.

At the highest frequency, He^+ ions are detected both on the left and the right of the image, corresponding to the weak transition to the $J = 0$ component of the spectrum drawn in red and the stronger transitions to the $J = 1, 2$ components of the spectrum drawn in blue, respectively.

To obtain a Doppler-free spectrum that combines the information contained in the spectra obtained from all selected detector areas, we use a cross-correlation method. All spectra in Fig. 3(a) consist of N data points $f(\nu_i) = f(i)$ with index $i = 0, 1, \ldots, N-1$ at frequencies $\nu_i = \nu_{\text{start}} + i\Delta\nu$. We evaluate the circular cross correlation R_{fg} between each spectrum and a periodically defined test function $g(\nu_i) = g(i)$ consisting of two Dirac delta distributions separated by a frequency interval $\nu_d = d\Delta\nu$ according to

$$R_{fg}(k) = \sum_{i=0}^{N-1} f(i)g(i+k)_{\text{mod N}}. \quad (1)$$

If ν_d does not match the Doppler splitting, each cross-correlation spectrum comprises four components of equal intensity per spectral line, because the cross-correlation leads to two lines separated by ν_d for each Doppler component. If ν_d exactly matches the Doppler splitting, the cross-correlation spectrum consists of two side bands separated by $2\nu_d$ and a central peak with double intensity at the Doppler-free position ν_0 [see spectra drawn in gray in Fig. 3(b)]. We calculate cross-correlation spectra for gradually increasing d values and determine, for all spectra in Fig. 3(a), the Doppler splittings numerically as the ν_d values corresponding to the cross-correlation spectra with maximal peak intensity. These cross-correlation spectra are depicted in gray in Fig. 3(b). Their sum, drawn in black, represents a Doppler-free spectrum to which *all* detected ions contribute, regardless of the Doppler shift. The sum spectrum also contains Doppler-broadened side bands. The central Doppler-free lines have full widths at half maximum of only $\approx$1.2 MHz. The large gain in signal-to-noise ratio resulting from the cross-correlation analysis is best recognized if one considers that the weak transition to the $(1s)(33p)\,^3P_0$ component is barely visible in the individual spectra of Fig. 3(a).

To extract the centroid transition frequencies of the $(1s)(np)\,^3P_{0-2} \leftarrow (1s)(2s)\,^3S_1$ transitions, we fit a sum of three Gaussian profiles, accounting for the three fine-structure components of the spectrum, with relative intensities of 5:3:1 for the $J = 2$, $J = 1$, and $J = 0$ components, respectively. The fit parameters describing the three-peak structure comprise the centroid frequency, the frequency differences between the peaks of the $J = 0$ and $J = 1$ and the $J = 1$ and $J = 2$ components, the maximum intensity, a linewidth determining the full width at half maximum (FWHM), and an overall background offset.

We measured transitions to two np Rydberg states with principal quantum numbers $n = 33$ and $n = 40$ and repeated the measurements 20 times for the $(1s)(33p)^3P_{0-2} \leftarrow (1s)(2s)^3S_1$ transition and 10 times for the $(1s)(40p)^3P_{0-2} \leftarrow (1s)(2s)^3S_1$ transition. Before each new measurement, we realigned the laser beam and its back reflection. In this way, we transformed a systematic error from a possible misalignment angle between the laser beam and its back reflection into a statistical error, as explained in Ref. [14].

The centroid transition frequency for a given transition is obtained as the weighted average of all measured spectra, and its statistical uncertainty is obtained from the weighted standard deviation of the averaged centroid frequency. The statistical uncertainties (112 and 174 kHz for the transitions to $n = 33p$ and $n = 40p$, respectively) are dominated by the residual first-order Doppler shift resulting from the uncertainty in the back-reflection angle.

We considered additional sources for systematic effects, as discussed in Ref. [14]. The photon-recoil shift and the second-order Doppler shift, 734 and -1.5 kHz, respectively, are subtracted from the measured transition frequencies to yield the corrected transition frequencies listed in Table I. Systematic uncertainties resulting from the pressure shift, dc-Stark shifts from the ≤ 1 mV/cm residual stray field, and the frequency calibration are negligible at our current precision. No change of the centroid transition frequencies could be detected when the excitation-laser power was reduced by a factor of 5, implying that ac-Stark shifts are also negligible. Momentum transfer by absorption of a photon from the incoming and reflected beam changes the transverse velocity by $\Delta v = (\pm h\nu)/m$, which affects the detection positions slightly [17]. Under our

TABLE I. Centroid transition frequencies for the $(1s)(33p)\,^3P_{0-2} \leftarrow (1s)(2s)\,^3S_1$ and $(1s)(40p)\,^3P_{0-2} \leftarrow (1s)(2s)\,^3S_1$ transitions, corrected for the photon-recoil shift and the second-order Doppler shift (second column), and centroid binding energies of the $(1s)(33p)\,^3P$ and $(1s)(40p)\,^3P$ Rydberg states, calculated using Eqs. (2) and (3) with the quantum-defect parameters taken from Ref. [16] (third column). Last column: Comparison of experimental and theoretical values of the ionization energies of the $(1s)(2s)\,^3S_1$ state.

	ν_{trans} (centroid)/MHz	E_{binding}/h (centroid)/MHz	$E_I/h\,(2\,^3S_1)$/(MHz)
$n = 33$	1149 809 632.350(112)	3033 110.473 33(11)	1152 842 742.823(113)
$n = 40$	1150 779 829.994(174)	2062 912.801 59(5)	1152 842 742.796(174)
Patkóš *et al.* [18]	n.a.	n.a.	1152 842 742.231(52)
Clausen *et al.* [14]	n.a.	n.a.	1152 842 742.640(32)

experimental conditions, this effect results in a shift of ≤ 1 kHz and can be neglected.

The ionization energy $E_I(2^3S_1)$ of the $(1s)(2s)\,^3S_1$ state of helium is determined by combining the experimental transition frequencies $\nu_n = E_n/h$ with the binding energy of the $33p$ and $40p$ Rydberg states given by the Rydberg-Ritz formula [19]

$$E_I(2\,^3S_1)/h = E_n/h + \frac{R_{\mathrm{He}} \cdot c}{(n^*)^2}, \tag{2}$$

where $R_{\mathrm{He}} = 109\,722.275\,548\,36(21)\ \mathrm{cm}^{-1}$ is the mass-corrected Rydberg constant calculated according to Ref. [20], and $n^* = n - \delta(n)$. The n-dependent quantum defect $\delta(n)$ is calculated iteratively using [21]

$$\delta(n) = \delta_0 + \frac{\delta_2}{[n-\delta(n)]^2} + \frac{\delta_4}{[n-\delta(n)]^4} + \frac{\delta_6}{[n-\delta(n)]^6} + \frac{\delta_8}{[n-\delta(n)]^8}, \tag{3}$$

with the quantum-defect parameters reported by Drake [16]. We independently verified the reliability of the quantum defects reported in Ref. [16] for the $J = 0$ fine-structure component, which is well resolved in our spectra.

Our new results for the ionization energy of the $2\,^3S_1$ state of ^{4}He* (see Table I) agree within the uncertainties with our previous experimental result [14], which was obtained by combining the ionization energy of the $2\,^1S_0$ state with the $2\,^1S_0 \leftarrow 2\,^3S_1$ interval measured by Rengelink *et al.* [22], but differ from the theoretical value by 592(124) ($n = 33$) and 538(182) kHz ($n = 40$), confirming the discrepancy between theory and experiment for this fundamental quantity noted earlier [14,18,23,24]. The calculations reported in Ref. [18] were the first to include the full $\alpha^7 m$ Lamb shift in a two-electron system and this discrepancy currently prevents the determination of the ^{4}He^{2+}-particle radius from He spectroscopy.

The method presented in this Letter features all advantages of Doppler-free spectroscopy by combining three elements: (i) Imaging enables the subdivision of the Doppler-broadened line profiles into a multitude of narrow sub-Doppler line profiles by selecting atoms or molecules belonging to different velocity classes; (ii) the retroreflection arrangement of the laser beam and the slight deviation from 90° of the laser and supersonic beams permit the determination of Doppler-free transition frequencies; and (iii) the cross-correlation analysis combines the sub-Doppler spectra into a Doppler-free spectrum to which all atoms or molecules in the sample contribute.

The method is not limited to the detection of Rydberg states by PFI. Without any change, it can be applied to resonance-enhanced two-photon ionization spectroscopy [(1 + 1) REMPI] in molecular beams, which is one of the most widely used techniques in molecular spectroscopy [25]. It can also be applied to laser-induced-fluorescence (LIF) spectroscopy [26], which is another very broadly used technique in molecular spectroscopy, if the spatial imaging of the ions is replaced by spatial imaging of the fluorescence. In the experiments presented here, we exploited spatial imaging to obtain sub-Doppler resolution. The spectral resolution could still be improved significantly by optimizing the ion-imaging optics and the gas-beam geometry. In this context, it is worth noting that the method might also find applications in a velocity-map-imaging [27] mode of dissociation products.

This work was supported by the Swiss National Science Foundation through the Sinergia-program (Grant No. CRSII5-183579) and a single-investigator grant (Grant No. 200020B-200478).

[1] T. W. Hänsch, Sub-Doppler spectroscopy, in *Atomic Physics, Proceedings of the Eighth International Conference on Atomic Physics, held August 2-6, 1982, at Chalmers University of Technology, Goteborg, Sweden*, edited by Ingvar Lindgren, Arne Rosén, and Sune Svanberg (Springer US, Boston, MA, 1983), Vol. 8, pp. 55–70, 10.1007/978-1-4684-4550-3.

[2] F. Biraben, The first decades of Doppler-free two-photon spectroscopy, C. R. Phys. **20**, 671 (2019).

[3] P. B. Changala, M. L. Weichman, K. F. Lee, M. E. Fermann, and J. Ye, Rovibrational quantum state resolution of the C_{60} fullerene, Science **363**, 49 (2019).

[4] A. Kortyna, D. M. B. Lesko, and D. J. Nesbitt, High-resolution sub-Doppler infrared spectroscopy of atmospherically relevant Criegee precursor CH_2I radicals: CH_2 stretch vibrations and "charge-sloshing" dynamics, J. Chem. Phys. **148**, 174308 (2018).

[5] W. Demtröder, Doppler-free laser spectroscopy, in *Handbook of High-Resolution Spectroscopy*, edited by M. Quack and F. Merkt (John Wiley & Sons, Chichester, 2011), Vol. 3, pp. 1759–1780, 10.1002/9780470749593.hrs082.

[6] L. Lynds and B. A. Woody, Sub-Doppler spectroscopy of ^{89}Y, J. Appl. Phys. **79**, 565 (1996).

[7] S. M. Shah Riyadh, H. Telfah, I. Jones, J. Bersson, C. Cheng, S.-M. Hu, D. Foote, and J. Liu, Mid-Infrared Doppler-free saturation absorption spectroscopy of the Q branch of CH_4 $\nu_3 = 1$ band using a rapid-scanning continuous-wave optical parametric oscillator, Opt. Open 22138301 (2023).

[8] M. L. Diouf, R. Tóbiás, T. S. van der Schaaf, F. M. J. Cozijn, E. J. Salumbides, A. G. Császár, and W. Ubachs, Ultra-precise relative energies in the (2 0 0) vibrational band of $H_2^{16}O$, Mol. Phys. **120**, e2050430 (2022).

[9] C. G. Parthey, A. Matveev, J. Alnis, B. Bernhardt, A. Beyer, R. Holzwarth, A. Maistrou, R. Pohl, K. Predehl, T. Udem, T. Wilken, N. Kolachevsky, M. Abgrall, D. Rovera, C. Salomon, P. Laurent, and T. W. Hänsch, Improved Measurement of the Hydrogen $1S - 2S$ Transition Frequency, Phys. Rev. Lett. **107**, 203001 (2011).

[10] A. Matveev *et al.*, Precision Measurement of the Hydrogen $1S-2S$ Frequency via a 920-km Fiber Link, Phys. Rev. Lett. **110**, 230801 (2013).

[11] R. K. Altmann, L. S. Dreissen, E. J. Salumbides, W. Ubachs, and K. S. E. Eikema, Deep-Ultraviolet Frequency Metrology of H_2 for Tests of Molecular Quantum Theory, Phys. Rev. Lett. **120**, 043204 (2018).

[12] S. A. Meek, A. Hipke, G. Guelachvili, T. W. Hänsch, and N. Picqué, Doppler-free Fourier transform spectroscopy, Opt. Lett. **43**, 162 (2018).

[13] D. W. Chandler and P. L. Houston, Two-dimensional imaging of state-selected photodissociation products detected by multiphoton ionization, J. Chem. Phys. **87**, 1445 (1987).

[14] G. Clausen, P. Jansen, S. Scheidegger, J. A. Agner, H. Schmutz, and F. Merkt, Ionization Energy of the Metastable 2^1S_0 State of ^{4}He from Rydberg-Series Extrapolation, Phys. Rev. Lett. **127**, 093001 (2021).

[15] D. Husmann *et al.*, SI-traceable frequency dissemination at 1572.06 nm in a stabilized fiber network with ring topology, Opt. Express **29**, 24592 (2021).

[16] G. W. F. Drake, High precision theory of atomic helium, Phys. Scr. T **83**, 83 (1999).

[17] J.-L. Wen, J.-D. Tang, J.-F. Dong, X.-J. Du, S.-M. Hu, and Y. R. Sun, Doppler-free spectroscopy of an atomic beam probed in traveling-wave fields, *Abstract, International Conference on Precision Physics and Fundamental Physical Constants FFK (2023). We thank Prof. Shui-Ming Hu, University of Science and Technology of China, Hefei, for drawing our attention to this systematic effect*.

[18] V. Patkóš, V. A. Yerokhin, and K. Pachucki, Complete $\alpha^7 m$ Lamb shift of helium triplet states, Phys. Rev. A **103**, 042809 (2021).

[19] W. Ritz, Zur Theorie der Serienspektren, Ann. Phys. (N.Y.) **317**, 264 (1903).

[20] E. Tiesinga, P. J. Mohr, D. B. Newell, and B. N. Taylor, CODATA recommended values of the fundamental physical constants: 2018, Rev. Mod. Phys. **93**, 025010 (2021).

[21] G. W. F. Drake and R. A. Swainson, Quantum defects and the $1/n$ dependence of Rydberg energies: Second-order polarization effects, Phys. Rev. A **44**, 5448–5459 (1991).

[22] R. J. Rengelink, Y. van der Werf, R. P. M. J. W. Notermans, R. Jannin, K. S. E. Eikema, M. D. Hoogerland, and W. Vassen, Precision spectroscopy of helium in a magic wavelength optical dipole trap, Nat. Phys. **14**, 1132 (2018).

[23] V. A. Yerokhin, V. Patkóš, and K. Pachucki, Relativistic Bethe logarithm for triplet states of helium-like ions, Eur. Phys. J. D **76**, 142 (2022).

[24] V. A. Yerokhin, V. Patkóš, and K. Pachucki, QED $m\alpha^7$ effects for triplet states of heliumlike ions, Phys. Rev. A **107**, 012810 (2023).

[25] M. N. R. Ashfold and C. M. Western, Multiphoton Spectroscopy, Applications, in *Encyclopedia of Spectroscopy and Spectrometry (Third Edition)*, edited by John C. Lindon, George E. Tranter, and David W. Koppenaal (Academic Press, Oxford, 2017), pp. 954–961.

[26] R. N. Zare, My life with LIF: A personal account of developing laser-induced fluorescence, Annu. Rev. Anal. Chem. **5**, 1 (2012).

[27] A. T. J. B. Eppink and D. H. Parker, Velocity map imaging of ions and electrons using electrostatic lenses: Application in photoelectron and photofragment ion imaging of molecular oxygen, Rev. Sci. Instrum. **68**, 3477 (1997).